photonics

MDPI

Article

Spectral-Kinetic Characterization of YF_3: Eu^{3+} and YF_3: (Eu^{3+}, Nd^{3+}) Nanoparticles for Optical Temperature Sensing

Ekaterina I. Oleynikova [1,*], Oleg A. Morozov [1,2], Stella L. Korableva [1] and Maksim S. Pudovkin [1,*]

[1] Institute of Physics, Kazan Federal University, 18 Kremlyovskaya str, Kazan 420008, Russia
[2] FRC Kazan Scientific Center of RAS, Sibirsky Trakt str. 10, Kazan 420029, Russia
* Correspondence: kate15-05@mail.ru (E.I.O.); jaz7778@list.ru (M.S.P.)

Abstract: YF_3: (Eu^{3+}, Nd^{3+}) nanoparticles (orthorhombic phase, D~130 nm) were synthesized via the co-precipitation method, with subsequent hydrothermal treatment and annealing. The Eu^{3+} τ_{decay} linearly descends with the increase of temperature in the 80–320 K range. The τ_{decay} (T) slope values of the annealed YF_3: Eu^{3+} (2.5 and 5.0 mol.%) nanoparticles were the highest ($110 \cdot 10^{-4}$ and $67 \cdot 10^{-4}$, μs/K) in the whole 80–320 K range, respectively. Thus, these samples were chosen for further doping with Nd^{3+}. The maximum S_a and S_r values based on the LIR (I_{Eu}/I_{Nd}) function were 0.067 K^{-1} (at 80 K) and 0.86%·K^{-1} (at 154 K), respectively. As mentioned above, the single-doped YF_3: Eu^{3+} (2.5%) nanoparticles showed the linearly decreasing τ_{decay} (T) function ($^5D_0$–$^7F_1$ emission). The main idea of Nd^{3+} co-doping was to increase this slope value (as well as the sensitivity) by increasing the rate of τ_{decay} (T) descent via the addition of one more temperature-dependent channel of $^5D_0$ excited state depopulation. Indeed, we managed to increase the slope (S_a) to $180 \cdot 10^{-4}$ K^{-1} at 80 K. This result is one of the highest compared to the world analogs.

Keywords: lifetime thermometry; Nd^{3+}/Yb^{3+}; Nd^{3+}/Yb^{3+}:YF_3; down-conversion; optical temperature sensors

check for updates

Citation: Oleynikova, E.I.; Morozov, O.A.; Korableva, S.L.; Pudovkin, M.S. Spectral-Kinetic Characterization of YF_3: Eu^{3+} and YF_3: (Eu^{3+}, Nd^{3+}) Nanoparticles for Optical Temperature Sensing. *Photonics* **2024**, *11*, 577. https://doi.org/10.3390/photonics11060577

Received: 16 May 2024
Revised: 7 June 2024
Accepted: 10 June 2024
Published: 20 June 2024

Copyright: © 2024 by the authors. Licensee MDPI, Basel, Switzerland. This article is an open access article distributed under the terms and conditions of the Creative Commons Attribution (CC BY) license (https://creativecommons.org/licenses/by/4.0/).

1. Introduction

Optical temperature sensing methods based on the use of inorganic phosphors have been intensively developed during the last decade [1]. In these methods, temperature reading is performed via analysis of the luminescence signal, which should be temperature-dependent. This approach is required in biology, medicine, and industry [2–4]. In turn, the temperature dependence of the luminescence signal should be known [5,6]. Among a huge variety of inorganic phosphors including oxides and quantum dots, rare-earth-doped fluoride nanoparticles play a special role due to high chemical and mechanical stability, bright narrow luminescence peaks [7], and, in some cases, low cytotoxicity [8,9]. Yttrium fluoride is considered a very promising host matrix, due to its low phonon energy (around 500 cm^{-1}), which leads to a decrease in the non-radiative transition probability. The water-based synthesis procedures are usually cheap, easy, and environmentally friendly. In addition, in this host, a high down-conversion quantum yield for rare-earth (RE) ion pairs was achieved [10]. The YF_3 matrix provides a substitution of Y^{3+} ions by RE^{3+} ones without valence change or charge compensation. Finally, in our previous work [11], we developed a hypothesis that the thermal expansion of YF_3 also contributes to the temperature sensitivity of the RE spectral-kinetic characteristics. Thus, it is interesting to study another ion pair in this promising matrix.

In turn, the choice of doping ion(s) is also a challenging task. Indeed, it depends on the application [7]; for medical applications, including hyperthermia, the phosphors should operate in the so-called biological window, where the biological tissues are partially transparent [11,12]. In the case of in vitro studies, excitation in this spectral range is also desirable because operation in the biological window provides a lack of autofluorescence

from cells. For industrial applications, such as temperature mapping of microcircuits, such strict restrictions are not so significant [13]. However, very important characteristics of the optical temperature sensors are absolute (S_a) and relative (S_r) temperature sensitivities. These characteristics express the rate of change of the luminescence parameters with the temperature [1]. A higher rate provides higher sensitivity, which leads to the easiness and accuracy of temperature measurements. In the case of single-doped phosphors, the temperature sensitivity of spectral characteristics is commonly based on the presence of two thermally coupled electron levels sharing their electron populations according to the Boltzmann law [5,6]. The main disadvantage of these systems is relatively low temperature sensitivity, depending on the energy gap between these two levels. Moreover, it is difficult to manipulate the energy gap due to the fact that the 4f electron shell is shielded by the 5s shell. To increase temperature sensitivity, double-doped phosphors can be utilized [5]. Indeed, there are more temperature-dependent processes that can synergize, increasing the temperature dependence of spectral-kinetic characteristics. One of the most common and interesting ways to increase the sensitivity is to analyze two emissions of heteronymous ions. However, these emissions should stem from two interacting energy levels. For example, in Tb^{3+}, Eu^{3+}:YF_3 phosphors, there are two pairs of interacting energy levels: $^5D_3$ (Tb^{3+})–$^5L_6$ (Eu^{3+}) and $^5D_4$ (Tb^{3+})–$^5D_1$ (Eu^{3+}) under Tb^{3+} excitation (377 nm corresponding to the $^7F_6$–$^5D_3$ absorption band of Tb^{3+}). In this case, the temperature-dependent parameter is the luminescence intensity ratio between the Tb^{3+}: $^5D_4 \rightarrow {}^7F_5$ transition (I_{542}) and the Eu^{3+}: $^5D_0 \rightarrow {}^7F_4$ one (I_{690}) [14]. The S_a was equal to 0.0013 in the 300–550 K temperature range. The efficiency of interaction between two levels rises with the temperature increase due to the phonon-assisted nature of this interaction. This fact explains the temperature sensitivity of the above-mentioned system. In turn, down-conversion optical temperature sensors based on Nd^{3+}/Yb^{3+} [15], Pr^{3+}/Yb^{3+}, and Er^{3+}/Yb^{3+} [16] ion pairs (where the first ion serves as a donor of energy) are also based on the same mechanism. In our previous work, we suggested that for Nd^{3+}/Yb^{3+}:YF_3 nanoparticles, the thermal expansion and, as a consequence, the decrease of distance between interacting ions also contribute to the temperature sensitivity of the spectral-kinetic characteristics [11]. After literature analysis, we concluded that the Eu^{3+}/Nd^{3+} system is capable of demonstrating notable temperature sensitivity under Eu^{3+} excitation [17]. Here, the interacting energy levels are $^5D_3$ (Eu^{3+})–$^2P_{1/2}$ (Nd^{3+}) and $^5D_0$ (Eu^{3+})–$^4G_{5/2}$ (Nd^{3+}) under Eu^{3+} excitation (λ_{exc} = 394 nm corresponding to the $^7F_0$–$^5L_6$ absorption band of Eu^{3+}). However, this system is significantly less studied compared to other ion pairs based on Eu^{3+} and Nd^{3+}. The objective of this work was to make a conclusion about the possible application of Eu^{3+}:YF_3 and Eu^{3+}, Nd^{3+}: YF_3 nanoparticles in optical temperature sensing, analyzing such characteristics as S_a and S_r. The tasks were:

- synthesis and physicochemical characterization of the samples (size, morphology, and phase composition);
- spectral-kinetic characterization to choose optimal Eu^{3+} and Nd^{3+} concentrations;
- spectral-kinetic characterization in order to understand the influence of the annealing procedure on spectral-kinetic characteristics; and
- the calculation of S_a and S_r.

2. Materials and Methods

2.1. Physicochemical Characterization of the Nanoparticles

The nanoparticles were synthesized via the co-precipitation method in distilled water with subsequent hydrothermal treatment [7,18]. The detailed synthesis procedure is described in our previous work devoted to rare-earth-doped YF_3 nanoparticles [11]. According to the work [19], the annealing of the obtained YF_3 nanoparticles at 400 °C in air does not lead to the formation of impurity phases; hence, we chose the annealing at 400 °C in air for 3 h. The phase composition of the samples was studied by means of X-ray diffraction (XRD) via Bruker D8 diffractometer with Cu K_α-radiation (Billerica, MA, USA). XRD simulation was carried out using VESTA software [20]. The morphology of the

samples was studied using a Hitachi HT7700 Exalens transmission electron microscope (TEM) with 100 kV accelerating voltage (TEM mode) (Tokyo, Japan). The average diameter of the nanoparticles was calculated from the 2D TEM images. Statistics were based on the analysis of 100 nanoparticles. To get the average diameter (D) of the nanoparticles, the area (in squire nanometers) of each nanoparticle from the TEM image was equated to the area of a circle ($\pi \cdot D^2/4$), where π = 3.14 and D is the diameter. The obtained histogram was approximated via the Lognornal function, where ± 1 standard deviation was determined.

2.2. Temperature-Dependent Spectral-Kinetic Characterization of the Nanoparticles

The excitation of the nanoparticles was performed via a LOTIS TII tunable laser LT-2211A (λ_{ex} (Eu^{3+}) = 394 nm (pulse duration and repetition were 10 ns and 10 Hz, respectively) (Minsk, Belarus). The spectra were recorded via a StellarNet (CCD) spectrometer (Tampa, FL, USA). The kinetic characterization was carried out via a monochromator connected with a photomultiplier tube FEU-62 and a digital oscilloscope (Rhode & Schwartz) with 1 GHz bandwidth (Munich, Germany). The experiments were performed in the 10–320 K temperature range via the so-called "cold finger" method. Temperature control was carried out via a thermostatic cooler from "CRYO Industries" with a LakeShore Model 325 (Westerville, OH, USA) temperature controller. The IR reflection measurements were carried out using a BrukerVertex80v Fourier spectrometer with near-normal ($\Theta \approx 15^\circ$) and oblique ($\Theta \approx 75^\circ$) light incidence on the sample at room temperature.

There are three molar concentration values of Eu^{3+}: 2.5, 5.0, and 7.5%. The choice of these concentrations was based on the decision to obtain the brightest Eu^{3+} luminescence. Indeed, at 1.0 mol.% the luminescence signal demonstrated low brightness, which is expected to be even lower after Nd^{3+} addition. In turn, the samples containing the above-mentioned concentrations demonstrated an opposite tendency. For the higher Eu^{3+} concentrations, the concentration quenching leads to a decrease in Eu^{3+} luminescence.

We synthesized 14 samples, listed in Table S1 of the Supplementary File. Briefly, there were three samples, (Eu^{3+}: 2.5, 5.0, and 7.5%):YF_3. Then, each sample was divided into two equal parts. One part was annealed and the second was not. Based on the obtained spectral-kinetic data, we selected four samples ((Eu^{3+}: 2.5 and 5.0%):YF_3, annealed, and not annealed). For these samples, we took several combinations of Eu^{3+}/Nd^{3+} and selected the most convenient ones for further study.

3. Results and Discussion

3.1. Physicochemical Characterization of the Nanoparticles

The phase composition of the YF_3-doped particles was confirmed via XRD. In particular, the normalized XRD patterns of YF_3: Eu^{3+} (2.5 mol.%) nanoparticles before and after annealing (400 °C, 4 h) and the YF_3 simulation are presented in Figure 1. In addition, the same normalized XRD patterns plotted in the same scale are presented in Figure S1 of the Supplementary File.

The XRD patterns of both samples located on one plot are presented in Figure S1 of the Supplementary File). The X-ray diffraction patterns are consistent with the simulation and the literature data and correspond to the orthorhombic structure of YF_3 [19,21] and to the number 01-070-1935 of the Inorganic Crystal Diffractions Database (ICDD) of orthorhombic YF_3 (*Pnma* space group). The well-defined YF_3 peaks, the absence of impurity, and amorphous phases are clearly seen. It can be seen from Figure 1 that the sample after annealing has narrower diffraction peaks. The XRD peak narrowing can be related to many factors, including the change in size and the removal of defects. Figure S1 illustrates more clearly the slight XRD peak sift after the annealing, which can also be related to the removal of defects, which affects the lattice parameters.

To investigate the contribution of the size to XRD peak narrowing, we performed the TEM imaging of the samples. Transmission electron microscopy (TEM) images of the YF_3: Eu^{3+} (2.5 mol.%) nanoparticles before (a) and after (b) annealing in air (400 °C, 4 h) are presented in Figures 2a and 2b, respectively.

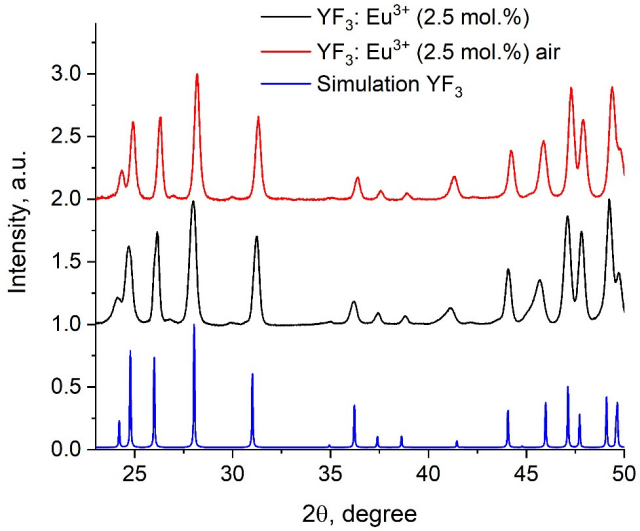

Figure 1. XRD patterns of YF_3: Eu^{3+} (2.5 mol.%) nanoparticles before (black) and after (red) annealing in air (400 °C, 4 h).

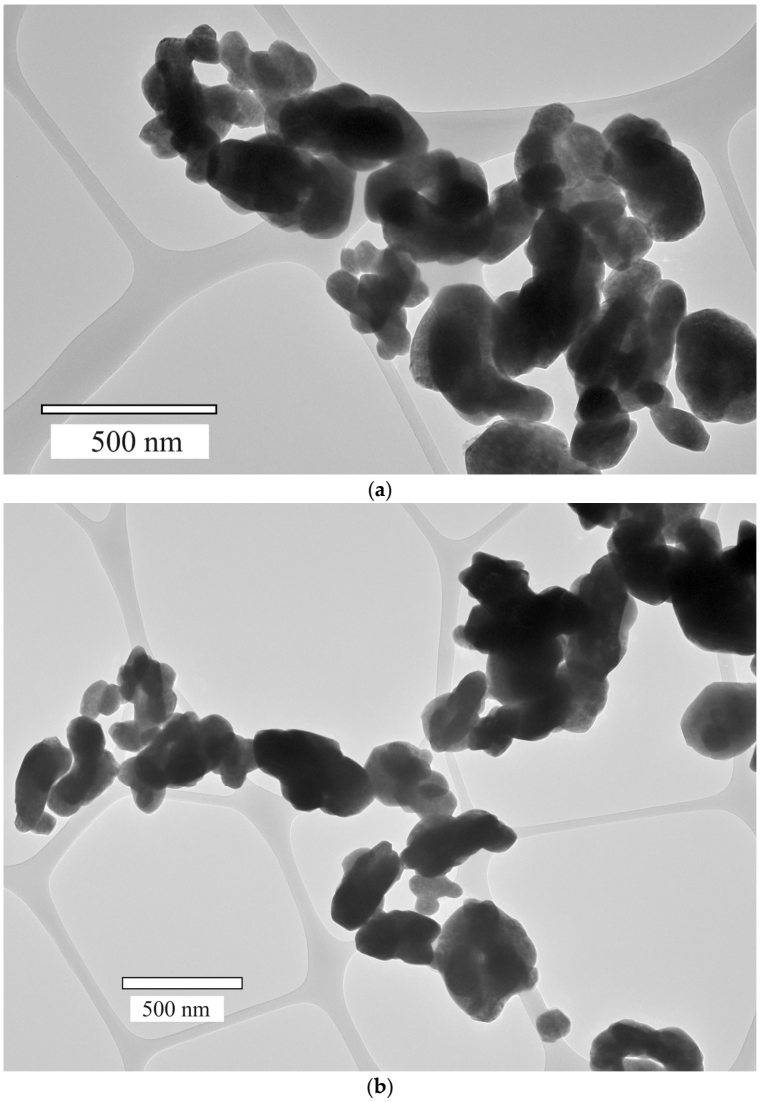

(**a**)

(**b**)

Figure 2. TEM image of YF_3: Eu^{3+} (2.5 mol.%) nanoparticles before (**a**) and after (**b**) annealing in air (400 °C, 4 h).

It can be seen that the annealing procedure does not affect the morphology of the nanoparticles. Specifically, both types of nanoparticles have a primary oval shape. The size distribution histograms of YF_3: Eu^{3+} (1 mol.%) nanoparticles before and after annealing are represented in Figures 3a and 3b, respectively.

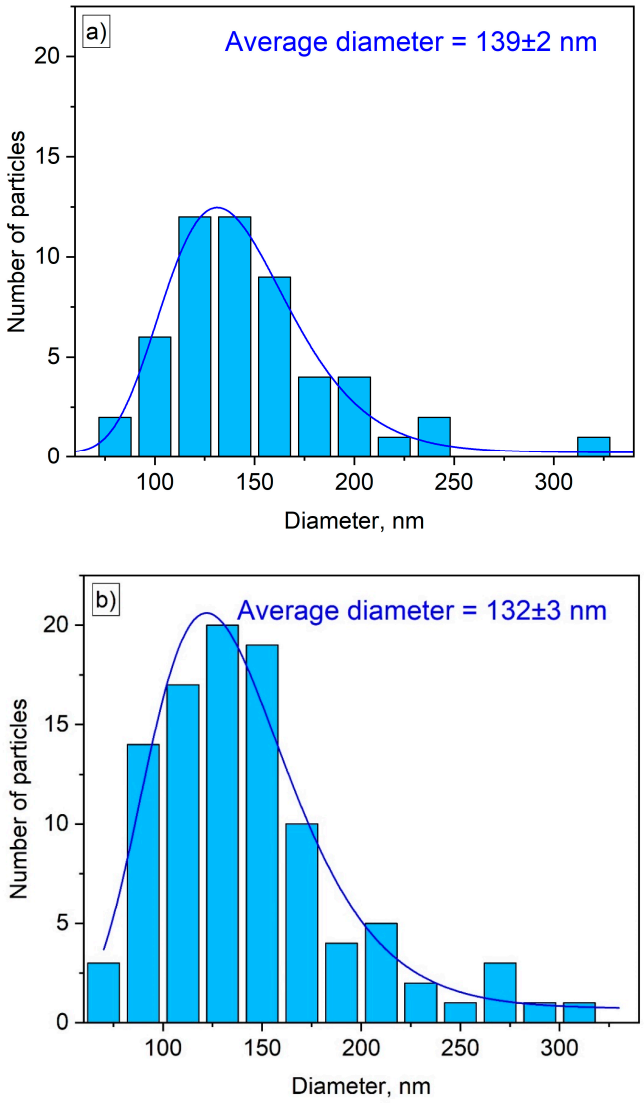

Figure 3. Size distribution histograms of YF_3: Eu^{3+} (2.5 mol.%) nanoparticles before (**a**) and after (**b**) annealing in air (400 °C, 4 h).

The size distribution histograms are not perfectly fitted by any peak functions, probably due to the non-spherical shape of the particles. However, the LogNormal approximation gives an estimation of the average size. The LogNormal fitting determined 139 ± 2 and 132 ± 3 nm average diameters before and after annealing, respectively. Regardless, the size of the particle is almost not changed. In addition, the diameter is larger than 15 nm; hence, the influence of the surface can be neglected [22]. Indeed, according to this work, the main unique difference between nanosized crystals and bulk ones is that the number of ions located on the surface of the nanoparticles and the number of ions located in the nanoparticle volume are comparable. The rare-earth ions located on the nanoparticle's surface have different ligand surroundings compared to the rare-earth ions inside the volume. The different surroundings lead to the different spectral-kinetic properties. However, according to the cited work in rare-earth trifluorides, for nanoparticles larger than 15 nm, the surface ions do not make a serious contribution to the spectral-kinetic properties in regards to

volume ions, and nanoparticles are more similar to bulk crystals in terms of spectral-kinetic properties. Since the size of the nanoparticles is almost not changed after the annealing, it can be suggested that the XRD peak narrowing can be related to the removal of defects (for instance, water molecules captured during the synthesis procedure [18,23]) after annealing. To verify this assumption, infrared (IR) spectroscopy was performed (Figure 4).

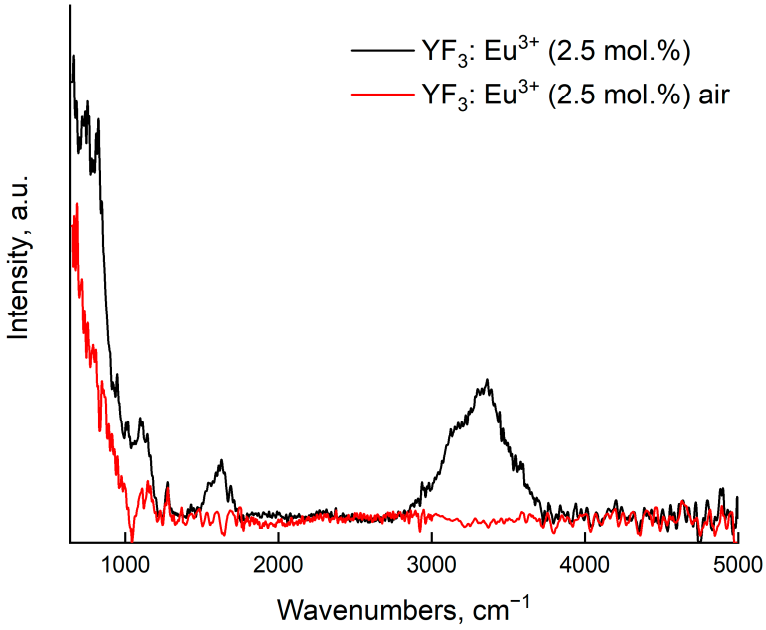

Figure 4. IR spectroscopy of Eu^{3+}: YF_3 nanoparticles before and after annealing in air (400 °C, 4 h).

The spectrum of the not-annealed sample demonstrates a wide band in the 2800–3750 cm^{-1} range. This peak corresponds to the stretching frequencies of the O–H groups of water molecules. The wide peak located between 1417 and 1800 cm^{-1} is also explained by fluctuations in the bonds of organic groups arising from the fluorinating agent. It can be concluded that the annealing procedure (400 °C, 4 h in air) is effective for the removal of the molecules cantoning OH groups. Finally, it can be suggested that the XRD peak narrowing can be related to the presence of such defects as captured water molecules. Indeed, the presence of additional impurities in the nanoparticle's volume leads to the formation of microstrain (the fluctuations of the distances between the interatomic lattice spacing). Finally, it can be concluded that the Eu^{3+}:YF_3 nanoparticles have a desirable orthorhombic phase composition. The annealing procedure (400 °C, 4 h) almost does not affect the diameter of the nanoparticles (139 ± 2 and 132 ± 3 nm before and after annealing, respectively), leading to water removal from the nanoparticles.

3.2. Temperature-Dependent Spectral-Kinetic Characterization of Single-Doped YF_3: Eu^{3+}

The energy level diagram of the Eu^{3+}/Nd^{3+} system is represented in Figure 5 (the Eu^{3+}–Nd^{3+} energy transfer will be discussed in the corresponding section). The optical excitation of Eu^{3+} is carried out at 394 nm ($^7F_0$–$^5L_6$ absorption band).

Further YF_3: Eu^{3+} (2.5; 5.0 and 7.5 mol.%) samples were synthesized, and the spectral and kinetic characteristics of YF_3: Eu^{3+} (2.5 mol.%) samples before and after annealing are shown in the Figures 6a and 6b, respectively.

It can be seen that the shape of the spectra is independent of the annealing procedure. In turn, the luminescence decay curves have a one-exponential character. The luminescence decay rate decreases after annealing. We also associate this phenomenon with the partial elimination of such defects as water molecules, as mentioned above. Thus, Eu^{3+} in the annealed samples has fewer channels of depopulating excited states. The temperature evolution of the annealed YF_3: Eu^{3+} (2.5 mol.%) luminescence spectra is presented in Figure 7.

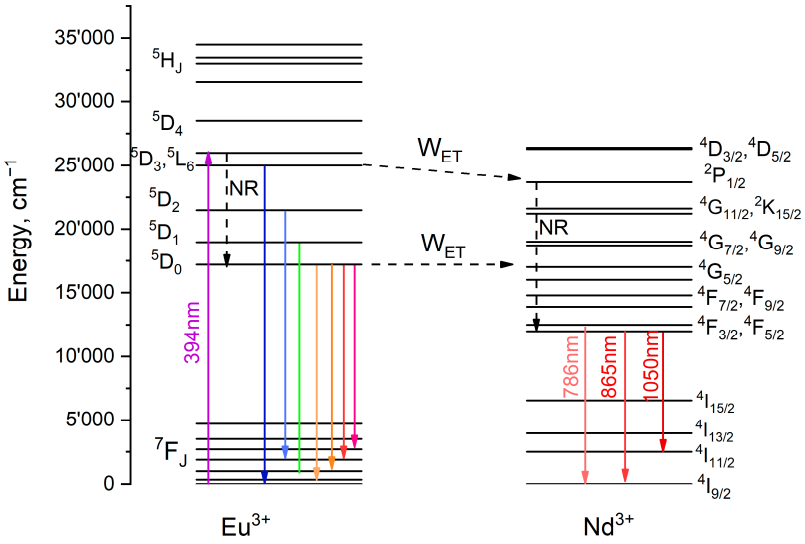

Figure 5. Energy level diagram of the Eu^{3+}/Nd^{3+} system. The optical excitation of Eu^{3+} is carried out at 394 nm ($^7F_0$–$^5L_6$ absorption band). NR–nonradiative transition, W_{ET}–energy transfer. Note: we did not observe the Nd^{3+} emission in single-doped YF_3: Nd^{3+} under 394 nm excitation.

It can be seen that the spectrum shape in the 570–750 nm range is independent of temperature. This phenomenon can be explained by the lack of thermally coupled electron levels in the Eu^{3+} energy level structure. After annealing, we did not observe a specific broadband luminescence, which was observed earlier in the YF_3 matrix [19]. The slight difference in spectral shape compared to Figure 6a can be explained by the use of different optical filters to remove the excitation wavelength. In order to characterize the weak temperature dependence of single-doped YF_3: Eu^{3+} (2.5%) nanoparticles in terms of quantity, we calculated the luminescence intensity ratio (LIR) of two Eu^{3+} peaks corresponding to $^5D_0$–$7F_1$ and $^5D_0$–$7F_2$ transitions (Figure S2 of the Supplementary File). The LIR demonstrates weak dependence on temperature, as was expected. The linear approximation gives the slope value around $(0.8 \pm 0.1)\cdot10^{-3}$ K^{-1}. This value is considered very low and can be compared to the analogs in Table 1.

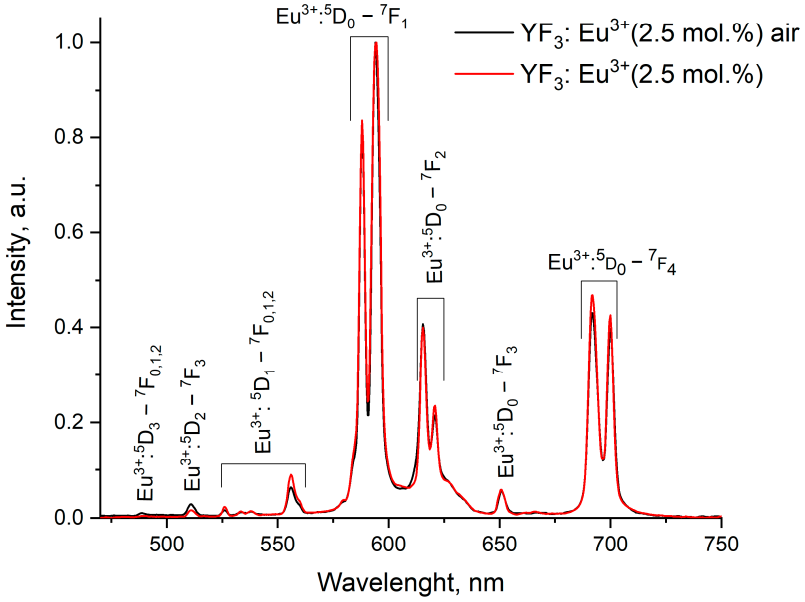

(**a**)

Figure 6. *Cont.*

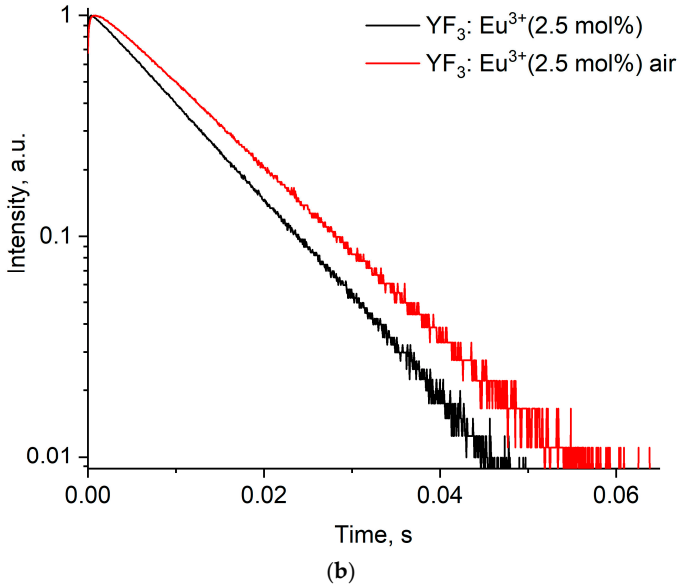

(**b**)

Figure 6. Room-temperature emission spectra (**a**) and luminescence decay curves (**b**) detected at 589.5 nm for YF_3: Eu^{3+} (2.5 mol.%) samples without annealing (black) and YF_3: Eu^{3+} (2.5 mol.%) annealed in air (red). The optical excitation of Eu^{3+} is carried out at 394 nm ($^7F_0$–$^5L_6$ absorption band).

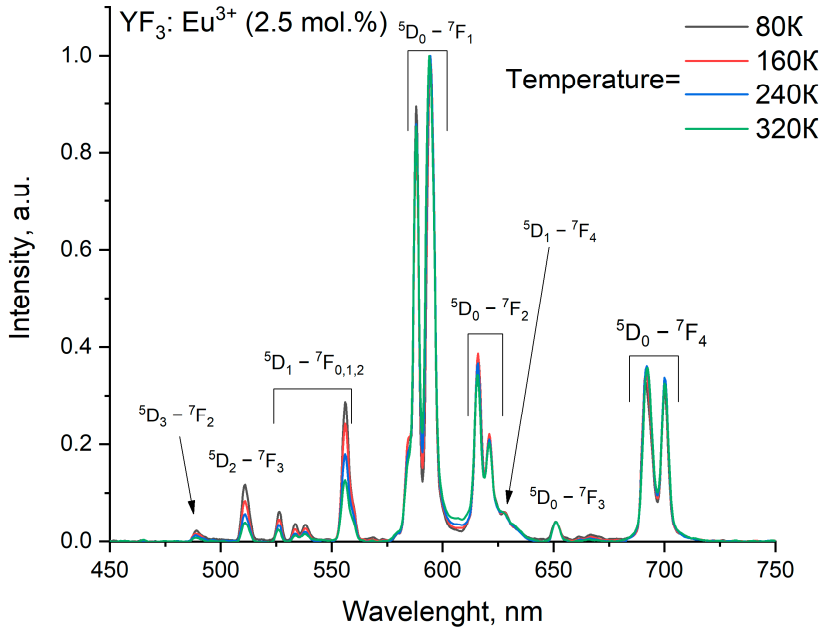

Figure 7. The normalized luminescence spectra of the annealed YF_3: Eu^{3+} (2.5%) nanoparticles detected in the 80–320 K temperature range. The optical excitation of Eu^{3+} is carried out at 394 nm ($^7F_0$–$^5L_6$ absorption band).

Table 1. The slope (μs/K) values of the luminescence decay time function of temperature, approximated with a linear function.

Sample	YF_3: Eu^{3+} 2.5%	YF_3: Eu^{3+} 5.0%	YF_3: Eu^{3+} 7.5%
Before annealing	$78 \cdot 10^{-4}$	$97 \cdot 10^{-4}$	$51 \cdot 10^{-4}$
After annealing	$110 \cdot 10^{-4}$	$67 \cdot 10^{-4}$	$17 \cdot 10^{-4}$

Figure 8 shows the luminescence decay time as a function of temperature in the 80–320 K temperature range. The corresponding luminescence decay time curves are presented in

Figure S3 of the Supplementary File. The decay time values are presented in Table S1 of the Supplementary File.

Figure 8 expresses the main tendency that the luminescence decay time linearly decreases with the increase in temperature. Usually, such a tendency is related to an increase in the probability of multiphonon relaxation with an increase in temperature. The same linear temperature dependence of luminescence decay time values for Pr^{3+} was observed in [24], which was also explained by multiphonon relaxation. However, the values of the slope for YF_3: Eu^{3+} nanoparticles are slightly higher compared to the above-mentioned Pr^{3+}-based phosphors. As discussed above, the annealed nanoparticles demonstrate higher values of decay time compared to the nanoparticles without annealing. The luminescence decay time values decrease with the increase of Eu^{3+} concentration, which can be explained by the concentration quenching. The slope values are presented in Table 1.

After annealing, the slope values decrease with the increase of Eu^{3+} concentration. Probably, the Eu^{3+} content influences the number of luminescence quenchers; hence, the contribution of temperature-dependent multiphonon relaxation in the temperature sensitivity of decay time decreases. For not-annealed YF_3: Eu^{3+} (5.0 and 7.5%) samples, the slope values are notably higher, which can be related to the increased number of quenchers. Here, the contribution of temperature-dependent multiphonon relaxation on these quenchers in the temperature sensitivity of decay time is higher. Nevertheless, the difference in the slope values requires additional investigation.

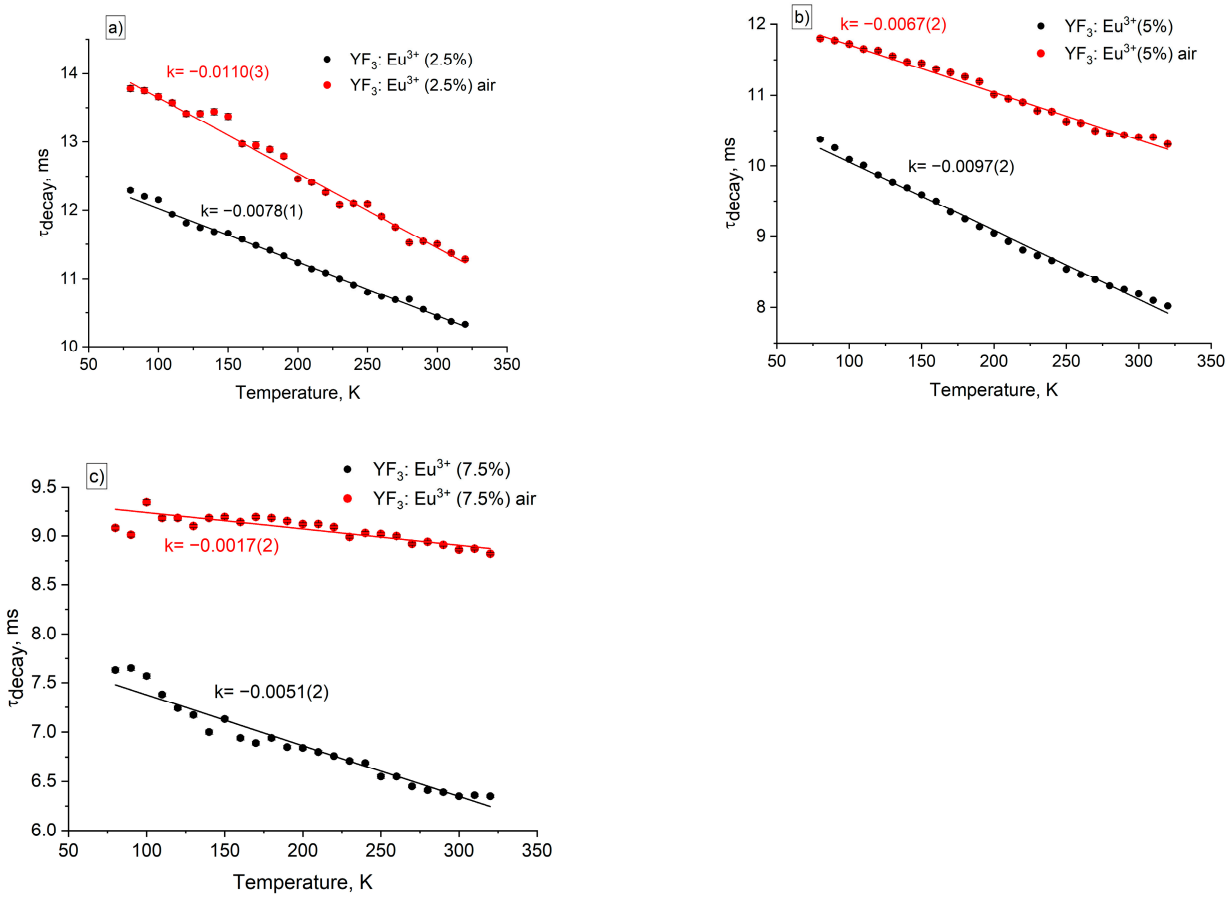

Figure 8. Luminescence decay time (τ_{decay}) at 589.5 nm ($^5D_0$–$^7F_1$ transition) for YF_3: Eu^{3+} (**a**) 2.5, (**b**) 5.0, and (**c**) 7.5 mol.% samples without annealing (black) and with annealing in air (red) in the 80–320 K temperature range. The data points were approximated with the linear function $\tau_{decay} = k \cdot T + b$, where k is the slope of the function.

3.3. Temperature-Dependent Spectral Characterization of Double-Doped YF_3:(Eu^{3+}, Nd^{3+})

For the purposes of temperature sensing, the high temperature dependence of luminescent parameters is desirable. In this case, the YF_3: Eu^{3+} (2.5 and 5.0%): annealed nanoparticles the slope of the τ_{decay} (T) function is the most pronounced (Table 1). We chose them for further doping with Nd^{3+} ions. Indeed, the addition of Nd^{3+} can lead to a more pronounced temperature dependence of the YF_3: Eu^{3+} spectral-kinetic characteristics. Specifically, it is suggested that Nd^{3+} provides an additional temperature-dependent channel of depopulation of the $^5D_0$ level of Eu^{3+}. Hence, some luminescence parameters of double-doped YF_3: (Eu^{3+}, Nd^{3+}) are expected to be more temperature-dependent. Since the electron level structure of both Eu^{3+} and Nd^{3+} ions is difficult, the $Eu^{3+} \rightarrow Nd^{3+}$ energy transfer process seems to be complex. However, according to the literature data, the energy transfer involves at least $^5D_3$ (Eu^{3+}) $\rightarrow$ $^2P_{1/2}$ (Nd^{3+}) and $^5D_0$ (Eu^{3+}) $\rightarrow$ $^4G_{5/2}$ (Nd^{3+}) energy transfer processes. We synthesized a set of samples which were also divided into two groups: before and after annealing. We did not observe the reliable signal of Nd^{3+} luminescence for all the not-annealed samples. This is probably related to the fact that some Nd^{3+} excited states are close to the vibrational states of OH groups. Among the different combinations of Nd^{3+} and Eu^{3+} in YF_3: Eu^{3+}, Nd^{3+} samples, it was difficult to obtain several samples with intense luminescence signals of both Nd^{3+} and Eu^{3+}, except for the YF_3: Eu^{3+} (2.5%), Nd^{3+} (4.0%) sample. The spectra of YF_3: Eu^{3+}, Nd^{3+} samples having different combinations of the doping ions are presented in Figure S4. Specifically, the room temperature spectra of the YF_3: (Eu^{3+} (2.5%), Nd^{3+} (4.0%)) before and after annealing are presented in Figure S4a of the Supplementary File). It can be seen that the Nd^{3+} luminescence is significantly less intense compared to the Eu^{3+} one for the not-annealed samples. After the annealing, the intensity of Nd^{3+} emission is higher. In turn, the annealed YF_3: (Eu^{3+} (2.5%), Nd^{3+} (2.0%)) sample demonstrated low intense Nd^{3+} luminescence under Eu^{3+} excitation. To increase the Nd^{3+} luminescence, we enlarged the Nd^{3+} concentration up to 4.0%. The room-temperature spectra of the annealed YF_3: (Eu^{3+} (2.5%), Nd^{3+} (4.0%)) and the luminescence decay curves of the $^5D_0$–$^7F_1$ transition of YF_3: (Eu^{3+} (2.5%), Nd^{3+} (0 and 4.0%)) are presented in Figures 9a and 9b, respectively.

It can be seen that the YF_3: (Eu^{3+} (2.5%), Nd^{3+} (4.0%)) sample has a relatively comparable intensity as some Eu^{3+} and Nd^{3+} peaks. There is a low-intensity peak of Nd^{3+} at 800 nm (from the excited $^4F_{5/2}$ state), which can be explained by the fact that $^4F_{5/2}$ and $^4F_{3/2}$ levels of Nd^{3+} are thermally coupled. However, the energy difference is around 1000 cm^{-1}, and the intensity of the emission from the higher energy $^4F_{5/2}$ levels is low in the studied 80–320 K temperature range [25]. The shape of the Eu^{3+} luminescence spectrum is slightly different compared to the single-doped (Eu^{3+}) samples, probably due to the presence of Nd^{3+}, which can quench some Eu^{3+} transitions. This sample was chosen for further temperature-dependent spectral-kinetic characterization. The rate of decay of the luminescence intensity significantly decreases with the addition of Nd^{3+} ion (4.0%) compared to the single-doped YF_3: Eu^{3+} (2.5%) sample. This observation suggests that there is an energy transfer from $^5D_0$ level (Eu^{3+}) to $^4G_{5/2}$ (Nd^{3+}). In order to provide higher temperature sensitivity of LIR (luminescence intensity ratio) function, we should take luminescence peaks that have an opposite dependence on temperature. For example, the $^5D_0$ (Eu^{3+}) $\rightarrow$ $^4G_{5/2}$ (Nd^{3+}) energy transfer is phonon-assisted. Hence, the population of $^4G_{5/2}$ of Nd^{3+} becomes more effective with the temperature increase via the depopulation of $^5D_0$ of Eu^{3+}. It can be concluded that the Eu^{3+} ($^5D_0$–$^7F_1$) intensity decreases with the temperature increase. In turn, the Nd^{3+} ($^4F_{3/2}$–$^4I_{9/2}$) demonstrated an opposite tendency. It should also be noted that the decay curve of the YF_3: (Eu^{3+} (2.5%), Nd^{3+} (4.0%)) sample is not single-exponential. It can be related to the fact that the Eu^{3+} ions are surrounded by different numbers of Nd^{3+} ions; hence, the rate of depopulation of Eu^{3+} surrounded with different numbers of Nd^{3+} ions is different, and the luminescence decay curve becomes

nonexponential. The integrated luminescence intensity ratio function (*LIR*) function can be determined as:

$$LIR = \frac{I_{Eu}}{I_{Nd}} \quad (1)$$

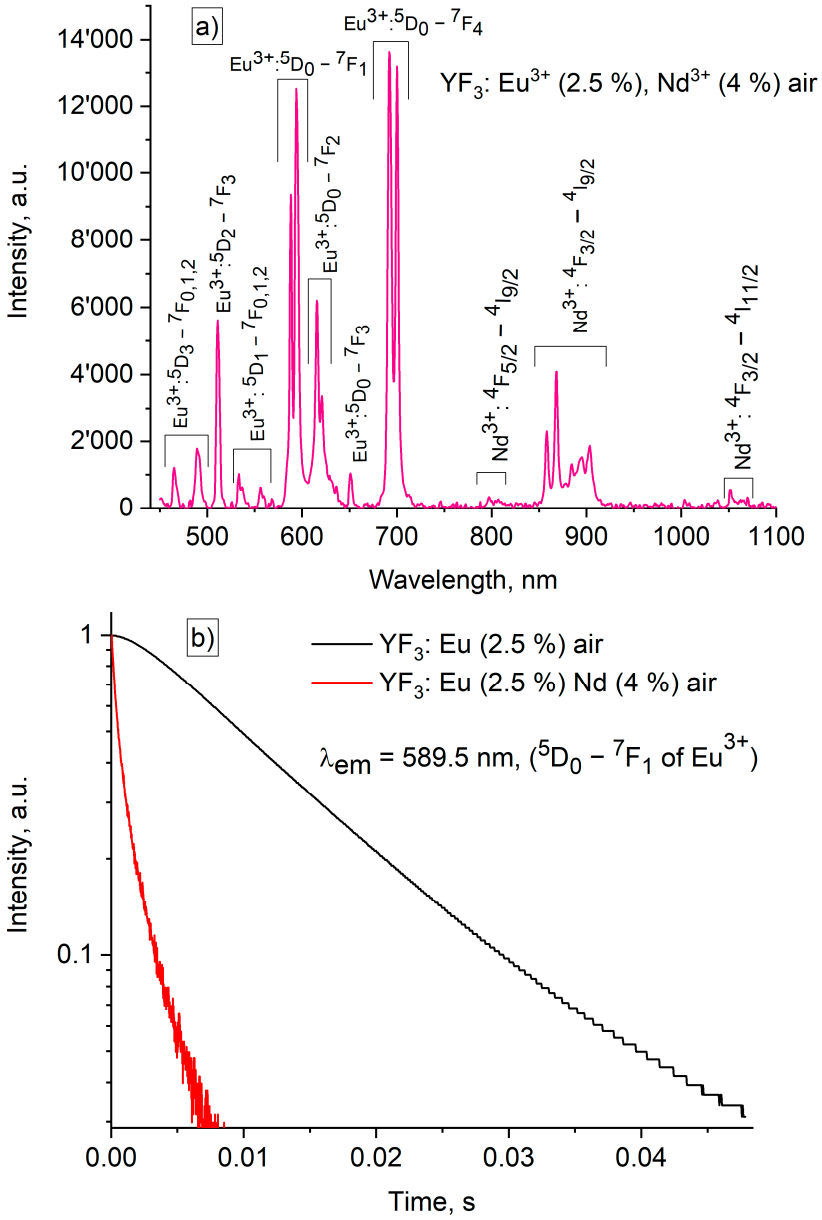

Figure 9. Room-temperature spectra of the annealed YF_3: (Eu^{3+} (2.5%), Nd^{3+} (4.0%)) (**a**) and luminescence decay curves of $^5D_0$–$^7F_1$ transitions of YF_3: (Eu^{3+} (2.5%), Nd^{3+} (0 and 4.0%)) (**b**). The optical excitation of Eu^{3+} is carried out at 394 nm ($^7F_0$–$^5L_6$ absorption band).

Additionally, the choice of LIR is illustrated in Figure S5 of the Supplementary File. In particular, the integrated intensities for Eu^{3+} and Nd^{3+} ions were taken in the ~570–605 and 845–925 nm ranges, respectively. The spectra detected in the 100–300 K range and the LIR function are represented in Figures 10a and 10b, respectively.

It can be seen that the LIR is a decay function, due to the above-mentioned opposite temperature dependence of both Eu^{3+} ($^5D_0$–$^7F_1$) and Nd^{3+} ($^4F_{3/2}$–$^4I_{9/2}$) emissions. Since the Eu^{3+}–Nd^{3+} energy transfer is not resonant, it involves the crystal lattice phonons.

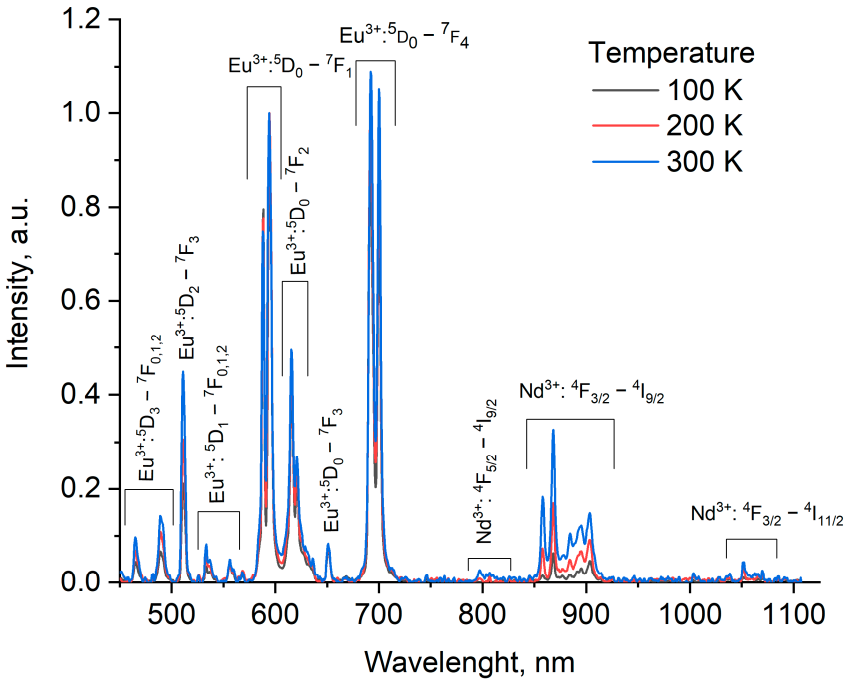

(**a**)

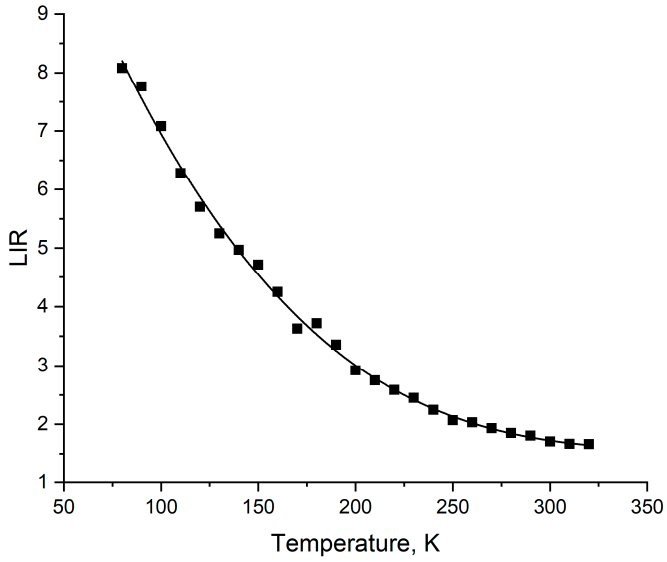

(**b**)

Figure 10. The luminescence spectra of the annealed YF_3: (Eu^{3+} (2.5%), Nd^{3+} (4.0 %)) sample (**a**) and *LIR* function of the YF_3: (Eu^{3+} (2.5%), Nd^{3+} (4.0 %)) sample (**b**).

The absolute (S_a) and relative (S_r) temperature sensitivities can be extracted from the LIR function using the following respective equations:

$$S_a = \left| \frac{d(LIR)}{dT} \right| \tag{2}$$

$$S_r = \frac{1}{LIR} \left| \frac{d(LIR)}{dT} \right| * 100\% \tag{3}$$

The S_a and S_r functions are presented in Figure 11.

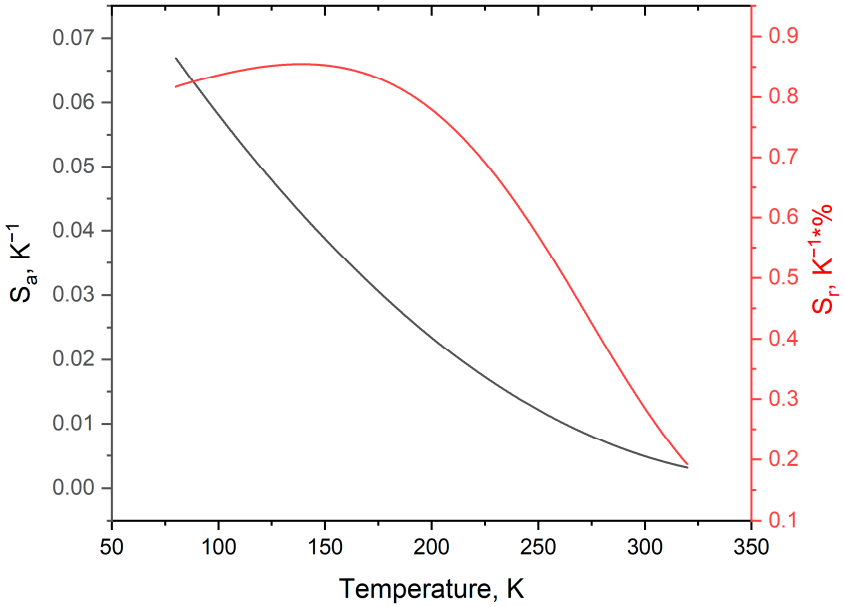

Figure 11. The S_a and S_r functions of the annealed YF_3: (Eu^{3+} (2.5%), Nd^{3+} (4.0%)) sample.

It can be seen that the highest sensitivity values are in the 80–200 K range. The obtained S_a and S_r values are quite competitive. Specifically, the list of world analogs is presented in Table 2.

Table 2. Comparison of luminescence thermometer performances of rare-earth-doped inorganic phosphors. *LIR* is taken as a temperature-dependent parameter.

Sample	Transitions and Wavelengths for LIR (I_1/I_2) and Optical Excitation Conditions	Maximum S_a [K^{-1}] in the 100–220 K Range	Maximum S_r [$\%K^{-1}$] in the 100–220 K Range	Ref.
Annealed YF_3: Eu^{3+}, Nd^{3+}	Nd^{3+} ($^4F_{3/2}$–$^4I_{9/2}$, ~866 nm), Eu^{3+} ($^5D_0$–$^7F_1$, ~590 nm) is carried out at 394 nm ($^7F_0$–$^5L_6$ absorption band)	0.065 (80 K)	0.85 (160 K)	This work
α-MoO_3: Eu^{3+}, Tb^{3+}	I_{Tb} ($^5D_4$–$^7F_5$, ~548 nm)/I_{Eu} ($^5D_0$–$^7F_2$, ~621 nm)	~10^{-3} at 105 K, not studied at higher temperatures	~ 0.50 at 105 K, not studied at higher temperatures	[26]
Tb^{3+}, Eu^{3+}: CaF_2	I_{Tb} ($^5D_4$–$^7F_5$, ~545 nm)/I_{Eu} ($^5D_0$–$^7F_2$, ~615 nm), λ_{ex} = 485 nm pulse laser	$4.0 \cdot 10^{-3}$	–	[27]
Tb^{3+} (6.0%), Eu^{3+} (8.0%): $Ca_5(PO_4)_3F$	I_{Tb} ($^5D_4$–$^7F_5$, ~548 nm)/I_{Eu} ($^5D_0$–$^7F_2$, ~621 nm), λ_{ex} = 299 nm, laser	$1.31 \cdot 10^{-3}$	0.40	[27]
Yb^{3+}, Tm^{3+}: $NaGdTiO_4$	I_{Tm} ($^3H_4$ (1) → $^3H_6$, 812 nm)/I_{Tm} ($^3H_4$ (2) → $^3H_6$, 798 nm), λ_{ex} = 980 nm, CW laser	$2.0 \cdot 10^{-3}$ at 100 K and $1.0 \cdot 10^{-3}$ at 200 K	–	[28]
Nd^{3+} (1%), Yb^{3+} (0.5–5%): $LiLaP_4O_{12}$	I_{Nd} ($^4F_{3/2}$–$^4I_{9/2}$, ~866 nm)/I_{Yb} ($^2F_{5/2}$–$^2F_{7/2}$, ~980 nm), λ_{ex} = 808 nm, CW laser	–	From 0.05 to 0.25 (depends on the Yb^{3+} concentration)	[29]

3.4. Temperature-Dependent Kinetic Characterization of Double-Doped YF_3: Eu^{3+}, Nd^{3+}

As mentioned above, the decay time of the $^5D_0$–$^7F_1$ (Eu^{3+}) emission of annealed single-doped YF_3: Eu^{3+} nanoparticles demonstrated the highest temperature sensitivity in the 80–320 K temperature range (Figure 8). It was suggested that the addition of Nd^{3+} can increase the temperature sensitivity of the decay time of the $^5D_0$–$^7F_1$ (Eu^{3+}) emission by providing an additional temperature-dependent channel depopulating the $^5D_0$ excited state of Eu^{3+}. Indeed, the Nd^{3+} significantly shortens the rate of luminescence decay (Figure 9), indicating the energy transfer from Eu^{3+} to Nd^{3+}. The $^5D_0$–$^7F_1$ (Eu^{3+}) luminescence decay curves of the YF_3: Eu^{3+} (2.5%), Nd^{3+} (4.0 %) sample are presented in Figure 12a.

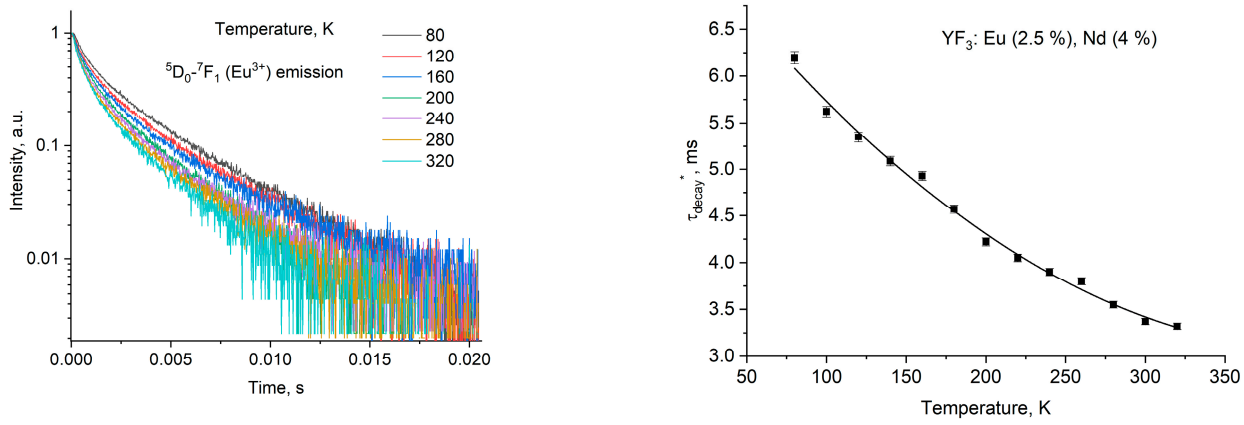

(**a**) (**b**)

Figure 12. The $^5D_0$–$^7F_1$ (Eu^{3+}) luminescence decay curves of the annealed YF_3: (Eu^{3+} (2.5%), Nd^{3+} (4.0%)) nanoparticles (**a**) and luminescence decay time (τ_{decay}*) as a function of temperature (**b**). Since the decay curves are nonexponential, the τ_{decay}* is taken as the time when the normalized luminescence intensity decreases from 1 to 0.1 a.u.

It can be seen that the curves are nonexponential in the whole temperature range. To compare the obtained decay time values of double-doped YF_3: (Eu^{3+}, Nd^{3+}) nanoparticles with single-doped YF_3: Eu^{3+} ones, we took τ_{decay}* as the time when the normalized luminescence intensity decreases from 1 to 0.1 a.u. The τ_{decay}* decreases with the temperature increase. This tendency is comparable to the observed for the LIR function (Figure 10) of the same sample. This can be explained by two factors: (1) nonradiative transitions, which provided the decreasing character of decay time-dependence for single-doped YF_3: Eu^{3+} samples; (2) the additional channel of Eu^{3+} depopulation by Nd^{3+} ions (phonon-assisted energy transfer). In this case, the probability of phonon appearance, and as a consequence, the efficiency of the Eu^{3+} decay (without Nd^{3+}) and Eu^{3+}–Nd^{3+} energy transfer, increases with the increase in temperature. However, the rate of both LIR and τ_{decay}* slightly decreases at elevated temperatures. It can be suggested that there is the activation of back energy transfer from Nd^{3+} to Eu^{3+}, which is observed for some donor/acceptor ion pairs at elevated temperatures [30]. The calculated S_a and S_r values are presented in Figure 13.

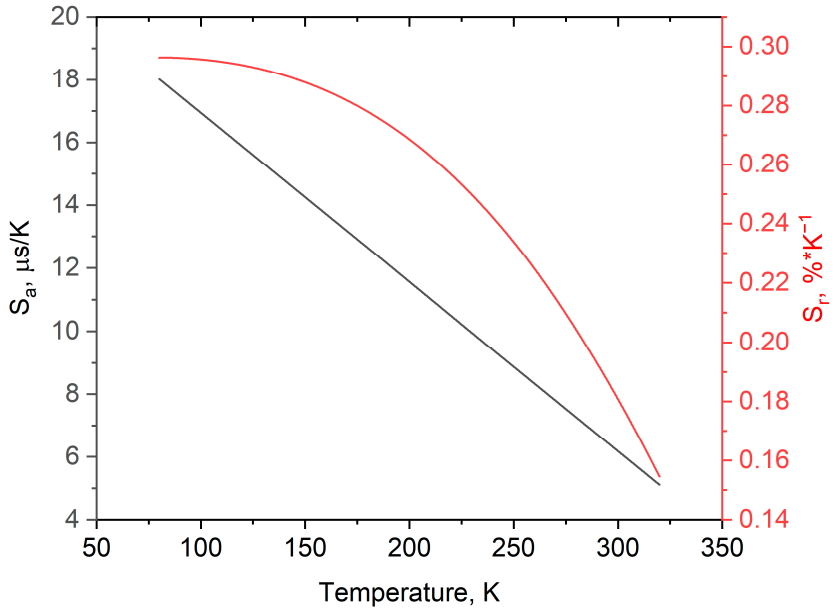

Figure 13. The S_a and S_r functions of the annealed YF_3: (Eu^{3+} (2.5%), Nd^{3+} (4.0%)) sample.

As mentioned above, the main idea of Nd^{3+} co-doping was to increase the temperature sensitivity of the $^5D_0$–$^7F_1$ (Eu^{3+}) luminescence decay time of the single-doped YF_3: Eu^{3+} (2.5%) nanoparticles. For the single-doped YF_3: Eu^{3+} (2.5%) nanoparticles, the decay time linearly decreases with the temperature increase. The slope is equal to 11.0 µs/K (note that, for the lineal dependence y = kx + b, the $S_a = |dy/dx|$ is equal to the slope value (k)). Indeed, we notably increased the S_a from in the 80–260 K temperature range. The comparison of the performances of rare-earth-doped inorganic temperature sensors are presented in Table 3.

Table 3. The comparison of the performances of rare-earth-doped inorganic temperature sensors. The luminescence decay time is taken as a temperature-dependent parameter.

Sample	Transition, Wavelength, and Excitation Conditions	Max S_a [µs/K]	Max S_r [%/K]	Ref.
Annealed YF_3: Eu^{3+}, Nd^{3+}	Emission of Eu^{3+} ($^5D_0$–$^7F_1$, ~590 nm), λ_{ex} = 394 nm ($^7F_0$–$^5L_6$ absorption band)	10–18 in the 80–200 K	0.2–0.3, in the 80–200 K	This work
β-$NaGdF_4$: Nd^{3+}, Yb^{3+}	Yb^{3+} ($^2F_{5/2}$–$^2F_{7/2}$, ~980 nm), λ_{ex} = 808 nm ($^4I_{9/2}$–$^4F_{5/2}$ abs. of Nd^{3+}).	Linear increase from 1.0 (300 K) to 2.8 (at 350 K)	Increases from 0.7 (300 K) to 1.6 (at 350 K)	[31]
$Nd_{0.5}RE_{0.4}Yb_{0.1}PO_4$ (RE = Y, Lu, La, Gd)	Yb^{3+} ($^2F_{5/2}$–$^2F_{7/2}$, ~980 nm), λ_{ex} = 940 nm, $^2F_{7/2}$–$^2F_{5/2}$ absorption band of Yb^{3+}.	0.4–1.6 at 300 K	0.5–1.2 at 300 K	[15]
$LiY_XYb_{1-X}F_4$: Tm^{3+}	λ_{ex} = 688 nm, $^3H_6$–$^3F_{2,3}$ (Tm^{3+}) absorption band of	1.2	0.36	[32]
β-PbF_2: Tm^{3+}, Yb^{3+}	Tm^{3+} ($^1G_4$–$^3H_6$, 478 nm), ($^2F_{7/2}$–$^2F_{5/2}$ abs. of Yb^{3+})	–	0.20 (at 300 K)	[33]
Gd_2O_2S: Eu^{3+}	Eu^{3+}, $^5D_0$ level, λ_{ex} = 375 nm (the transition is not specified)	–	Linear decreas: 4.5 (at 280 K) to 3.0 (AT 335 K)	[34]
$LaGdO_3$: Er^{3+}/Yb^{3+}	Er^{3+} ($^4S_{3/2}$–$^4I_{15/2}$, 530 nm), ($^4F_{9/2}$–$^4I_{15/2}$, 670 nm) ($^2F_{7/2}$–$^2F_{5/2}$ abs. of Yb^{3+})	–	1.79 ($^4S_{3/2}$) and 0.94 ($^4F_{9/2}$) in the 290–350 K range.	[35]
TiO_2: Sm^{3+}	Sm^{3+} ($^4G_{5/2}$–$^6H_{7/2}$, 612 nm) 438 nm (matrix excitation)		10%/°C at 70 °C	[36]
$NaPr(PO_3)_4$	Pr^{3+} (emission from $^3P_0$, the wavelength is not specified), λ_{ex} = 488 nm ($^3H_4$–$^3P_0$ absorption band of Pr^{3+}.		Linearl increas: $44{\cdot}10^{-4}$ (at 300 K) to $60{\cdot}10^{-4}$ (at 365 K)	[24]
$LaPO_4$: Nd^{3+}, Er^{3+}	Nd^{3+} ($^4F_{5/2}$–$^4F_{11/2}$ λ_{em} = 1055 nm), λ_{ex} = 808 nm abs. $^4I_{9/2}$–$^4F_{5/2}$)	Max value 0.003 at 600 K	max value ~2.5 at 600 K	[37]
MOF: Eu^{3+}	Host excitation under 368 nm, λ_{em} = 525 nm	Linear decrease: ~550 us (at 270 K) to ~460 us (at 360 K). The estimated S_a is equal to 1.0 us/K	–	[38]
GAG: Mn^{3+}, Mn^{4+}	λ_{ex} = 266 nm, λ_{em} = 610 nm ($^5T_2$–$^5E''$ of Mn^{3+})		2.08 at 249 K	[39]
Pr^{3+}: YAG	Pr^3+ ($^1D_2$–$^3H_4$, 617 nm), λ_{ex} = 488 nm ($^3H_4$–$^3P_0$ absorption band of Pr^{3+}.	Linear decrease: ~190 us (at 10 K) to ~110 us (at 1000 K). The estimated S_a is equal to 0.080 us/K	–	[40]
CaF_2: Ho^{3+}	Ho^{3+} ($^5F_5$–$^5I_8$, λ_{em} = 650 nm), λ_{ex} = 488 nm ($^5F_3$–$^5I_8$ absorption band of Ho^{3+}.	Linear decrease: ~100 us (at 100 K) to ~40 us (at 450 K). The estimated S_a is equal to 0.17 us/K	–	[40]
$LiPr(PO_3)_4$	Pr^{3+} (emission from $^3P_0$, the wavelength is not specified) λ_{ex} = 488 nm ($^3H_4$–$^3P_0$ absorption band of Pr^{3+}.	0.0044 K^{-1} in the 300–365 K range	The S_a increases almost linearly from 0.44%/K (at 300 K) to 0.65%/K (at 365 K)	[24]

It can be concluded that the studied YF_3: (Eu^{3+}, Nd^{3+}) sample demonstrates the highest S_a values, as well as competitive S_r ones, especially in the 80–200 K range. Many of the above-mentioned phosphors do not demonstrate such competitive S_r values in this

temperature range or their optical characteristics were not studied. Hence, the optical temperature sensors operating in this range are highly demanded in cryogenic industries.

We also calculated the temperature uncertainly for the annealed YF_3: (Eu^{3+} (2.5%), Nd^{3+} (4.0%) sample according to:

$$\delta T = \frac{1}{S_r} \cdot \frac{\sigma_{LIR}}{LIR(T_0)} \quad (4)$$

where σ_{LIR} is the standard deviation, T_0 is the temperature at which uncertainty was calculated by repetitive measurements (8 times), and S_r is the above-mentioned relative temperature sensitivity [%·K^{-1}]. The δT, as the function of temperature, is presented in Figure 14.

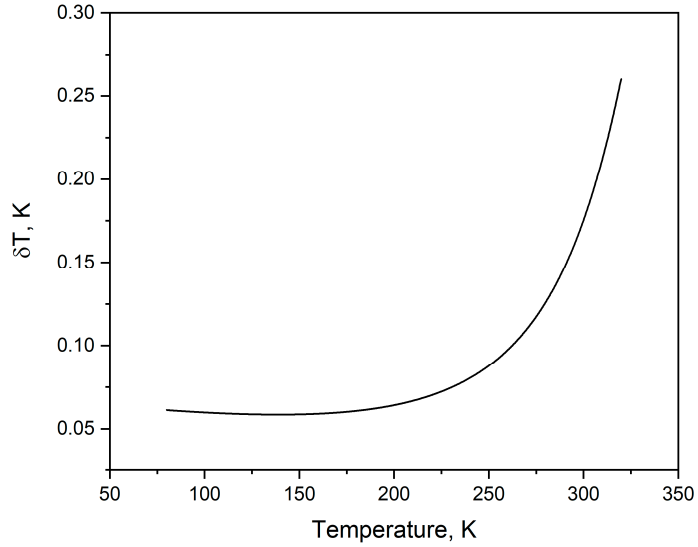

Figure 14. Temperature resolution plot of the annealed YF_3: (Eu^{3+} (2.5%), Nd^{3+} (4.0%) sample.

The values of δT are in the 0.02–0.25 K range. The obtained values of δT are comparable to the (nowadays) luminescent temperature sensors [1]. We also checked the stability of the sensors by measuring decay characteristics 8 times, changing the temperature from 80 to 320 K. The kinetic curves did not differ between each other. This was expected for inorganic fluoride matrices, including the studied YF_3 one.

4. Conclusions

The YF_3: (Eu^{3+}, Nd^{3+}) nanoparticles were synthesized via the co-precipitation method in distilled water with subsequent hydrothermal treatment. Then, the powders were divided into two groups: not annealed and annealed at 400 °C in air for 4 h. The phase composition of the YF_3 doped particles was confirmed via XRD. In particular, XRD patterns correspond to the orthorhombic structure of the YF_3 host matrix without impurity and amorphous phases. After the annealing procedure, the samples have narrower diffraction peaks. According to the TEM imaging, the annealing procedure insignificantly affects the morphology of the nanoparticles. The average diameter was determined as 139 ± 2 and 132 ± 3 nm before and after annealing, respectively. The IR spectroscopy showed the presence of water in the not-annealed nanoparticles. In turn, after annealing, the presence of the water was not observed. It was suggested that the narrowing of the XRD peaks is related to the removal of water and to the improvement of nanoparticle crystallinity. The annealing procedure does not affect the shape of the luminescence spectrum of YF_3: Eu^{3+} (2.5, 5.0, and 7.5 mol.%) nanoparticles. In addition, the spectrum shape of these samples is independent of temperature in the 80–320 K range. However, after annealing, the luminescence decay time (τ_{decay}) increases. The τ_{decay} linearly descends with the increase in temperature. The slope values of the annealed YF_3: Eu^{3+} (2.5 and 5.0 mol.%)

nanoparticles were the highest ($110 \cdot 10^{-4}$ and $67 \cdot 10^{-4}$ μs/K in the whole 80–320 K range, respectively); thus, these samples were chosen for further doping with Nd^{3+}. Moreover, the obtained slope value $110 \cdot 10^{-4}$ μs/K (S_a) is very competitive, surpassing many counterparts. We synthesized a set of YF_3: (Eu^{3+} (2.5 and 5.0 mol.%), Nd^{3+} (2.0, 4.0 mol.%)) annealed and not-annealed samples. In the case of the not-annealed samples, the Nd^{3+} emission intensity was negligible compared to the Eu^{3+} one for all the samples. This was explained by the fact that water molecules quench Nd^{3+} emission because the Nd^{3+} excited states are resonant to some vibrational states of OH groups. In turn, the annealed samples shoved more intense Nd^{3+} emission under Eu^{3+} excitation. In particular, the YF_3: (Eu^{3+} (2.5%), Nd^{3+} (4.0%)) sample demonstrated the highest Nd^{3+} intensity and was chosen for further LIR (I_{Eu}/I_{Nd}) characterization. The maximum S_a and S_r values based on the LIR function were 0.067 K^{-1} (at 80 K) and 0.86%·K^{-1} (at 154 K), respectively. As mentioned above, the single-doped YF_3: Eu^{3+} (2.5%) nanoparticles showed the linearly decreasing τ_{decay} (T) function ($^5D_0$–$^7F_1$ emission) with the slope value of $110 \cdot 10^{-4}$ μs/K. The main idea of Nd^{3+} co-doping was to increase this slope value by increasing the rate of τ_{decay} (T) descent via the addition of one more temperature-dependent channel of $^5D_0$ excited state depopulation. Indeed, we managed to increase the slope up to $180 \cdot 10^{-4}$ μs/K at 80 K and to obtain a very competitive value of S_r = 0.3%/K at 80 K. This result is one of the highest compared to the world analogs.

It should also be noted that the annealing is a crucial step in the synthesis procedure because, after the annealing, the Nd^{3+} emission can be observed, unlike the not-annealed nanoparticles. According to IR spectroscopy, the annealing procedure removes the water from the nanoparticles, which can be considered as the main quencher of IR Nd^{3+} emission. For this reason, the Sa and Sr were not calculated for not-annealed double-doped YF_3: (Eu^{3+}, Nd^{3+}) nanoparticles.

Finally, it can be concluded that the relatively new Eu^{3+}/Nd^{3+} donor/acceptor ion pairs showed very competitive performances via both LIR and luminescence decay time dependencies on temperature in the visible spectral range. This paves the way toward submicron temperature mapping and time-resolved temperature sensing in broad temperature ranges, including physiological ones. The notable temperature sensitivities at liquid nitrogen temperatures make the studied phosphors promising for the space industry.

Supplementary Materials: The following supporting information can be downloaded at: https://www.mdpi.com/article/10.3390/photonics11060577/s1, Figures S1–S5. Table S1.

Author Contributions: Conceptualization, M.S.P. and E.I.O.; methodology, M.S.P., S.L.K., E.I.O. and O.A.M.; software O.A.M., investigation, M.S.P., S.L.K., E.I.O. and O.A.M.; resources, M.S.P.; data curation, M.S.P., S.L.K., E.I.O. and O.A.M.; M.S.P. and E.I.O.; project administration, M.S.P.; funding acquisition, M.S.P. All authors have read and agreed to the published version of the manuscript.

Funding: The research was funded by a grant from the Russian Science Foundation, number 22-72-00129, https://rscf.ru/project/22-72-00129/ (accessed on 7 June 2024).

Institutional Review Board Statement: Not applicable.

Informed Consent Statement: Not applicable.

Data Availability Statement: The original contributions presented in the study are included in the article/supplementary material, further inquiries can be directed to the corresponding author/s.

Conflicts of Interest: The authors declare no conflicts of interest.

References

1. Dramićanin, M.D. Trends in luminescence thermometry. *J. Appl. Phys.* **2020**, *128*, 040902. [CrossRef]
2. Xu, H.; Bai, G.; He, K.; Tao, S.; Lu, Z.; Zhang, Y.; Xu, S. Multifunctional optical sensing applications of luminescent ions doped perovskite structured $LaGaO_3$ phosphors in near-infrared spectroscopy. *Mater. Today Phys.* **2022**, *28*, 100872. [CrossRef]
3. Wang, C.; Meng, Y.; Su, Z.; Dong, J.; Lian, Y.; Huang, Y.; Bai, G. Self-monitored Nd-doped $MoSe_2$ nanosheets with near-infrared luminescent sensing for photothermal therapy. *J. Mater.* **2024**, *10*, 163–172. [CrossRef]

4. Luo, Y.; Li, H.; Cai, M.; Liu, Y.; Chen, L.; Xu, S.; Bai, G. Designing polyacrylic acid capped luminescent rare earth core–shell nanoparticles for simultaneous Cu (II) and temperature sensing. *Mater. Des.* **2022**, *224*, 111405. [CrossRef]
5. Brites, C.D.; Balabhadra, S.; Carlos, L.D. Lanthanide-based thermometers: At the cutting-edge of luminescence thermometry. *Adv. Opt. Mater.* **2019**, *7*, 1801239. [CrossRef]
6. Brites, C.D.S.; Millán, A.; Carlos, L.D. Lanthanides in luminescent thermometry. In *Handbook on the Physics and Chemistry of Rare Earths*; Elsevier: Amsterdam, The Netherlands, 2016; Volume 49, pp. 339–427.
7. Fedorov, P.P.; Luginina, A.A.; Kuznetsov, S.V.; Osiko, V.V. Nanofluorides. *J. Fluor. Chem.* **2011**, *132*, 1012–1039. [CrossRef]
8. Pudovkin, M.S.; Shamsutdinov, N.I.; Zelenikhin, P.V.; Nizamutdinov, A.S. Transmission electron microscopy and flow cytometry study of cellular uptake of unmodified Pr^{3+}:LaF_3 nanoparticles in dynamic. *J. Nanopart. Res.* **2021**, *23*, 124. [CrossRef]
9. Pudovkin, M.S.; Zelenikhin, P.V.; Shtyreva, V.V.; Evtugyn, V.G.; Salnikov, V.V.; Nizamutdinov, A.S.; Semashko, V.V. Cellular uptake and cytotoxicity of unmodified Pr^{3+}: LaF_3 nanoparticles. *J. Nanopart. Res.* **2019**, *21*, 1–13. [CrossRef]
10. Meijer, J.M.; Aarts, L.; van der Ende, B.M.; Vlugt, T.J.; Meijerink, A. Downconversion for solar cells in YF_3: Nd^{3+}, Yb^{3+}. *Phys. Rev. B* **2010**, *81*, 035107. [CrossRef]
11. Pudovkin, M.; Oleynikova, E.; Kiiamov, A.; Cherosov, M.; Gafurov, M. Nd^{3+}, Yb^{3+}: YF_3 Optical Temperature Nanosensors Operating in the Biological Windows. *Materials* **2022**, *16*, 39. [CrossRef]
12. Piñol, R.; Brites, C.D.; Silva, N.J.; Carlos, L.D.; Millán, A. Nanoscale thermometry for hyperthermia applications. In *Nanomaterials for Magnetic and Optical Hyperthermia Applications*; Elsevier: Amsterdam, The Netherlands, 2019; pp. 139–172.
13. Jaque, D.; Vetrone, F. Luminescence nanothermometry. *Nanoscale* **2012**, *4*, 4301–4326. [CrossRef]
14. Chen, D.; Wang, Z.; Zhou, Y.; Huang, P.; Ji, Z. Tb^{3+}/Eu^{3+}: YF_3 nanophase embedded glass ceramics: Structural characterization, tunable luminescence and temperature sensing behavior. *J. Alloys Compd.* **2015**, *646*, 339–344. [CrossRef]
15. Maciejewska, K.; Bednarkiewicz, A.; Marciniak, L. NIR luminescence lifetime nanothermometry based on phonon assisted Yb^{3+}–Nd^{3+} energy transfer. *Nanoscale Adv.* **2021**, *3*, 4918–4925. [CrossRef]
16. Kaczmarek, A.M.; Kaczmarek, M.K.; Van Deun, R. Er^{3+}-to-Yb^{3+} and Pr^{3+}-to-Yb^{3+} energy transfer for highly efficient near-infrared cryogenic optical temperature sensing. *Nanoscale* **2019**, *11*, 833–837. [CrossRef]
17. Qi, Y.; Li, S.; Min, Q.; Lu, W.; Xu, X.; Zhou, D.; Yu, X. Optical temperature sensing properties of KLu_2F_7: Yb^{3+}/Er^{3+}/Nd^{3+} nanoparticles under NIR excitation. *J. Alloys Compd.* **2018**, *742*, 497–503. [CrossRef]
18. Alakshin, E.M.; Klochkov, A.V.; Kondratyeva, E.I.; Korableva, S.L.; Kiiamov, A.G.; Nuzhina, D.S.; Kodjikian, S. Microwave-assisted hydrothermal synthesis and annealing of DyF_3 nanoparticles. *J. Nanomater.* **2016**, *2016*, 7148307. [CrossRef]
19. Tan, M.C.; Kumar, G.A.; Riman, R.E.; Brik, M.G.; Brown, E.; Hommerich, U. Synthesis and optical properties of infrared-emitting YF_3:Nd nanoparticles. *J. Appl. Phys.* **2009**, *106*, 063118. [CrossRef]
20. Momma, K.; Izumi, F. VESTA 3 for three-dimensional visualization of crystal, volumetric and morphology data. *J. Appl. Crystallogr.* **2011**, *44*, 1272–1276. [CrossRef]
21. Wang, X.; Sheng, T.; Fu, Z.; Li, W. Highly uniform YF_3: Ln^{3+} (Ln = Ce^{3+}, Tb^{3+}) walnut-like microcrystals: Hydrothermal synthesis and luminescent properties. *Mater. Res. Bull.* **2013**, *48*, 2143–2148. [CrossRef]
22. Vanetsev, A.; Kaldvee, K.; Puust, L.; Keevend, K.; Nefedova, A.; Fedorenko, S.; Orlovskii, Y. Relation of Crystallinity and Fluorescent Properties of LaF_3: Nd^{3+} Nanoparticles Synthesized with Different Water-Based Techniques. *ChemistrySelect* **2017**, *2*, 4874–4881. [CrossRef]
23. Alakshin, E.M.; Blokhin, D.S.; Sabitova, A.M.; Klochkov, A.V.; Klochkov, V.V.E.; Kono, K.; Tagirov, M.S. Experimental proof of the existence of water clusters in fullerene-like PrF_3 nanoparticles. *JETP Lett.* **2012**, *96*, 181–183. [CrossRef]
24. Gharouel, S.; Labrador-Páez, L.; Haro-González, P.; Horchani-Naifer, K.; Férid, M. Fluorescence intensity ratio and lifetime thermometry of praseodymium phosphates for temperature sensing. *J. Lumin.* **2018**, *201*, 372–383. [CrossRef]
25. Laia, A.S.; Hora, D.A.; Rezende, M.V.d.S.; Gomes, M.A.; Brandão-Silva, A.C.; dos Santos, M.A.C.; Dantas, N.O.; Silva, A.C.A.; Rodrigues, J.J.; Valerio, M.E.G.; et al. Investigating the Thermometric Performance of Inorganic Materials Doped with Nd^{3+} under Infrared LED Excitation: An Alternative for Deep Tissue Luminescent Thermometry. *Photonics* **2023**, *10*, 485. [CrossRef]
26. Liu, J.; Van Deun, R.; Kaczmarek, A.M. Eu^{3+}, Tb^{3+}-and Er^{3+}, Yb^{3+}-doped α-MoO_3 nanosheets for optical luminescent thermometry. *Nanomaterials* **2019**, *9*, 646. [CrossRef]
27. Fangfang, H.U.; Zhangmei, Z.H.A.O.; Fengfeng, C.H.I.; Xiantao, W.; Min, Y.I.N. Structural characterization and temperature-dependent luminescence of CaF_2: Tb^{3+}/Eu^{3+} glass ceramics. *J. Rare Earths* **2017**, *35*, 536–541.
28. Zhou, A.; Song, F.; Song, F.; Feng, M.; Adnan, K.; Ju, D.; Wang, X. Optical thermometry using fluorescence intensities multi-ratios in $NaGdTiO_4$: Yb^{3+}/Tm^{3+} phosphors. *Opt. Mater.* **2018**, *78*, 438–444. [CrossRef]
29. Tan, M.; Li, F.; Cao, N.; Li, H.; Wang, X.; Zhang, C.; Chen, G. Accurate in vivo nanothermometry through NIR-II lanthanide luminescence lifetime. *Small* **2020**, *16*, 2004118. [CrossRef]
30. Marciniak, L.; Bednarkiewicz, A.; Stefanski, M.; Tomala, R.; Hreniak, D.; Strek, W. Near infrared absorbing near infrared emitting highly-sensitive luminescent nanothermometer based on Nd^{3+} to Yb^{3+} energy transfer. *Phys. Chem. Chem. Phys.* **2015**, *17*, 24315–24321. [CrossRef]
31. Ji, Z.; Cheng, Y.; Cui, X.; Lin, H.; Xu, J.; Wang, Y. Heating-induced abnormal increase in Yb^{3+} excited state lifetime and its potential application in lifetime luminescence nanothermometry. *Inorg. Chem. Front.* **2019**, *6*, 110–116. [CrossRef]
32. Khadiev, A.R.; Korableva, S.L.; Ginkel, A.K.; Morozov, O.A.; Nizamutdinov, A.S.; Semashko, V.V.; Pudovkin, M.S. Down-conversion based Tm^{3+}: $LiY_{1-X}Yb_XF_4$ temperature sensors. *Opt. Mater.* **2022**, *134*, 113118. [CrossRef]

33. Fu, Y.; Zhao, L.; Guo, Y.; Yu, H. Up-conversion luminescence lifetime thermometry based on the $^{1}G_{4}$ state of Tm^{3+} modulated by cross relaxation processes. *Dalton Trans.* **2019**, *48*, 16034–16040. [CrossRef]
34. Katumo, N.; Gao, G.; Laufer, F.; Richards, B.S.; Howard, I.A. Smartphone-based luminescent thermometry via temperature-sensitive delayed fluorescence from Gd_2O_2S: Eu^{3+}. *Adv. Opt. Mater.* **2020**, *8*, 2000507. [CrossRef]
35. Siaï, A.; Haro-González, P.; Naifer, K.H.; Férid, M. Optical temperature sensing of Er^{3+}/Yb^{3+} doped $LaGdO_3$ based on fluorescence intensity ratio and lifetime thermometry. *Opt. Mater.* **2018**, *76*, 34–41. [CrossRef]
36. Dramićanin, M.D.; Antić, Ž.; Ćulubrk, S.; Ahrenkiel, S.P.; Nedeljković, J.M. Self-referenced luminescence thermometry with Sm^{3+} doped TiO_2 nanoparticles. *Nanotechnology* **2014**, *25*, 485501. [CrossRef]
37. Maciejewska, K.; Bednarkiewicz, A.; Marciniak, L. The influence of the Er^{3+} dopant concentration in $LaPO_4$: Nd^{3+}, Er^{3+} on thermometric properties of ratiometric and kinetic-based luminescent thermometers operating in NIR II and NIR III optical windows. *Phys. B Condens. Matter* **2021**, *620*, 413247. [CrossRef]
38. Zhou, Y.; Yan, B. Ratiometric detection of temperature using responsive dual-emissive MOF hybrids. *J. Mater. Chem. C* **2015**, *3*, 9353–9358. [CrossRef]
39. Marciniak, L.; Trejgis, K. Luminescence lifetime thermometry with Mn^{3+}–Mn^{4+} co-doped nanocrystals. *J. Mater. Chem. C* **2018**, *6*, 7092–7100. [CrossRef]
40. Kamma, I.; Kommidi, P.; Reddy, B.R. High temperature measurement using luminescence of Pr^{3+} doped YAG and Ho^{3+} doped CaF_2. *Phys. Status Solidi C* **2009**, *6*, S187–S190. [CrossRef]

Disclaimer/Publisher's Note: The statements, opinions and data contained in all publications are solely those of the individual author(s) and contributor(s) and not of MDPI and/or the editor(s). MDPI and/or the editor(s) disclaim responsibility for any injury to people or property resulting from any ideas, methods, instructions or products referred to in the content.